Nanoscale

How nanoscale surface steps promote ice growth on feldspar: microscopy observation of morphology-enhanced condensation and freezing

Journal:	*Nanoscale*
Manuscript ID	NR-ART-10-2019-008729
Article Type:	Paper
Date Submitted by the Author:	11-Oct-2019
Complete List of Authors:	Friddle, Ray; Sandia National Laboratories California, Thürmer, Konrad; Sandia National Laboratories California

ARTICLE

How nanoscale surface steps promote ice growth on feldspar: microscopy observation of morphology-enhanced condensation and freezing

Received 00th January 20xx,
Accepted 00th January 20xx

DOI: 10.1039/x0xx00000x

Raymond W. Friddle[a] and Konrad Thürmer[a]

Ice in the atmosphere affects Earth's radiative properties and initiates most precipitation. Growing ice often requires a solid surface, either to catalyze freezing of supercooled cloud droplets or to serve as a substrate for ice deposited from water vapor. There is evidence that this surface is typically provided by airborne mineral dust; but how chemistry, structure and morphology interrelate to determine the ice-nucleating ability of mineral surfaces remains elusive. Here, we combine optical microscopy with atomic force microscopy to explore the mechanisms of initial ice growth on alkali feldspar, a mineral proposed to dominate ice nucleation in Earth's atmosphere. When cold air becomes supersaturated with respect to water, we discovered that ice rapidly spreads along steps of a feldspar surface. By measuring how ice propagation depends on surface-step height we establish a scenario where supercooled liquid water condenses at steps without having to overcome a nucleation barrier, and subsequently freezes quickly. Our results imply that steps, which are common even on macroscopically flat feldspar surfaces, can accelerate water condensation followed by freezing, thus promoting glaciation and dehydration of mixed-phase clouds.

Introduction

The formation[i] of ice in the atmosphere plays a key role in determining Earth's weather and climate.[1,2] The extent of ice clouds, for example, as well as the ice content of mixed-phase clouds have a direct effect on Earth's radiation balance.[3,4,5,6] But more importantly, most precipitation [1,2] including rain [3,7,8] is initiated by atmospheric ice formation. Ice can emerge in the atmosphere via various microscopic processes [1,2,9,10]; some require the presence of a foreign material (heterogenous ice nucleation) while others proceed unaided by a foreign substance (homogeneous nucleation). Homogeneous ice nucleation can be observed at a measurable rate only below ≈-36°C, where it takes place via freezing of supercooled cloud droplets. For ice nucleation to occur at higher temperatures, a suitable foreign particle must provide a surface onto which an ice nucleus can grow to a critical size without being impeded by an insurmountable activation barrier. Soot, bacteria, pollen, fungal spores, metal and metal oxide particles all have been implicated as substrates promoting ice nucleation.[1,10,11] Recent studies, however, agree that on a global scale, heterogeneous ice nucleation is dominated by airborne mineral dust.[11,12,13,14,15] While past research has often focused on ubiquitous clay aerosols, interest has shifted recently toward aerosols of alkali feldspars (hereafter used interchangeably with feldspars), shown to be more efficient ice nucleators.[16,17,18,19]

Surface structure, morphology, defects, particle size, and chemical functional groups, modified by varying degrees of atmospheric processing,[20,21,22] have been proposed to determine the ice-nucleating ability of mineral surfaces; but our current understanding of the role of these individual properties and how they interact in an atmospheric setting remains unsettled.[1,10,23,24,25,26,27,28] Progress has been impeded, in part, by a lack of insight from direct microscopy observation. For example, macroscopic measurements of nucleation rates often cannot distinguish between various nucleation mechanisms without ambiguity.[1,9,10,26] Case in point are past observations interpreted as deposition nucleation, i.e., ice nucleation from vapor onto a substrate without prior formation of liquid water.[9] Marcolli[29] and David et al.[30] argue that many of those observations can be explained by initial condensation of liquid water in pores between aggregated particles, followed by freezing. Here, the capillary effect of a concave pore surface allows condensation of liquid water at a relative humidity RH_w < 100%. In the pursuit of revealing the mechanisms of ice nucleation, recent environmental scanning electron microscopy (ESEM) studies[31,32,33] demonstrated the power of direct microscopic observation. Wang et al.,[32] for example, reported that ice prefers to nucleate at the edges of stacked kaolinite platelets while avoiding their basal planes. When growing ice on feldspar at low supersaturation with respect

[a] Sandia National Laboratories, Livermore, CA 94550
Email: rwfridd@sandia.gov, kthurme@sandia.gov
†Electronic Supplementary Information (ESI) available: Experimental methods, image analysis procedure, detailed AFM topographical map, Movies S1-S6.
DOI: 10.1039/x0xx00000x

to ice, as typical for cirrus clouds, Kiselev *et al.*[33] discovered that ice preferentially nucleates on high-energy microfacets of (100) orientation.

To be able to address these questions we developed an experimental approach capable of monitoring ice growth nondestructively as well as characterizing surface steps in detail. We pre-record maps of substrate morphology at sub-nanometer height resolution with atomic force microscopy (AFM) before tracking ice evolution with an optical camera. Ice is grown onto K-feldspar (orthoclase) substrates under realistic atmospheric conditions in a custom-made environmental chamber at atmospheric pressure (see Fig. S1). AFM images of the feldspar (001) surface (Figs. 1A, 2A, 2B, S3, and S4) show steps of varying direction and ranging in height from sub-nanometer to multiple micrometers.

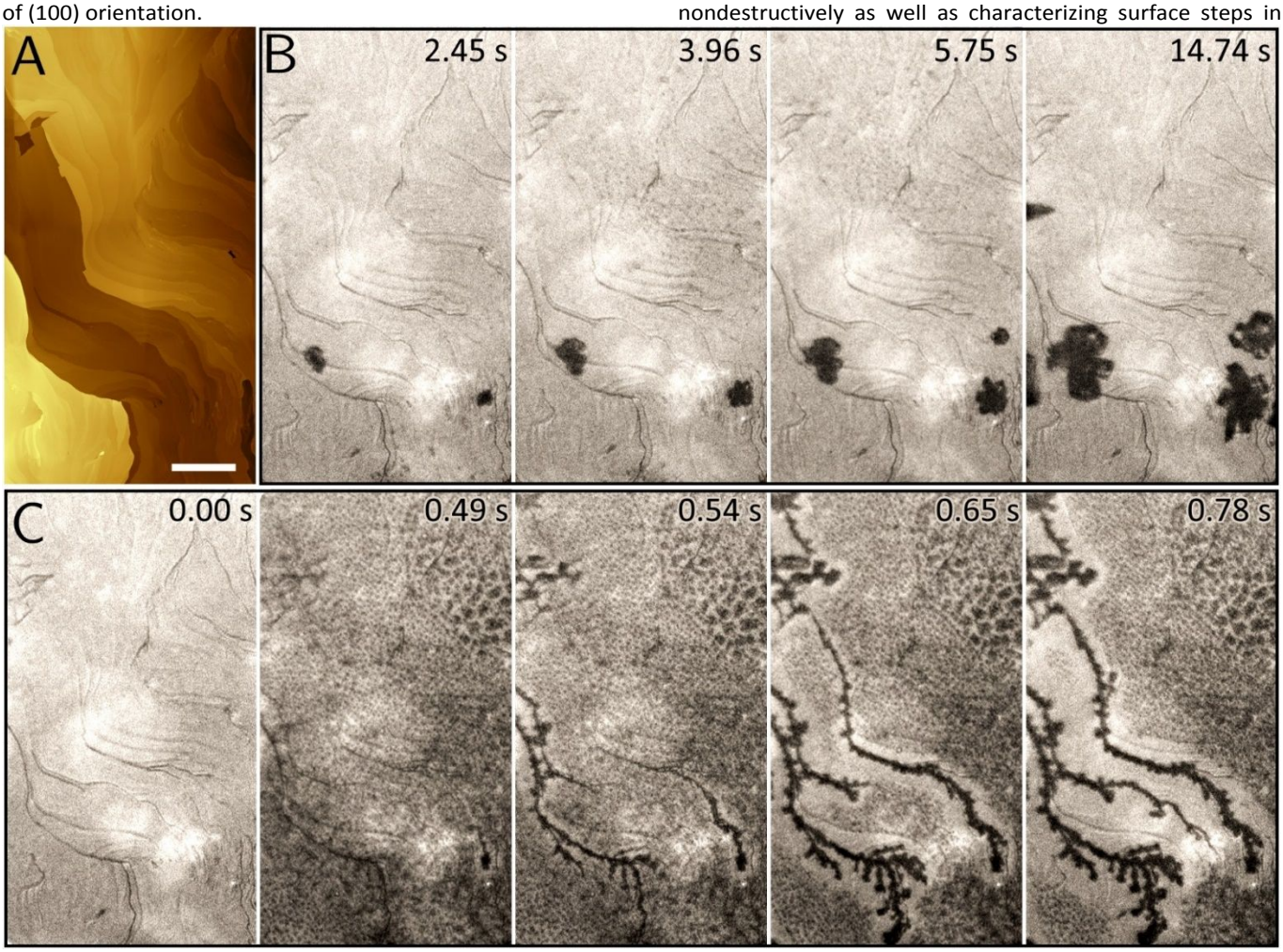

Fig. 1. Two modes of ice growth on feldspar. Image sequences acquired with optical microscopy reveal two growth modes at T= -30°C. (A) AFM surface morphology map of the same field of view (FOV) examined optically (scale bar 50 µm). (B) Below saturation (RH_w= 100 %) for our system (AH_{in}=0.45 g/m^3), few dispersed ice nuclei (dark) emerge and grow slowly. (C) At higher humidity (AH_{in}=0.75 g/m^3), once an ice nucleus has formed, ice spreads rapidly along surface steps of the feldspar substrate. (These two experiments are shown at a larger FOV in ESI† Movies S1 and S2).

Our work now extends microscopy observations to higher humidities, as found in mixed-phase clouds, seeking insight into the interplay between liquid and solid water in the presence of a feldspar surface. But unlike past experiments that mimic the freezing of mineral dust-containing cloud droplets upon cooling,[16,19,34] we examine how feldspar interacts with initially dry cold air upon raising its humidity above saturation with respect to liquid water (RH_w> 100 %). Cavities, common in clay aerosols, have been proposed[29,30,35,36] to allow condensation of liquid water below saturation (RH_w< 100 %) due to the capillary effect of a concave surface ("inverse Kelvin effect"). If cavities are absent, can surface steps adopt their role when air becomes saturated, by providing a location where water can attach without having to overcome a nucleation barrier? Since steps are ubiquitous on solid surfaces, condensation of supercooled water at steps could thus be important for initiating ice formation in the atmosphere.

Experimental

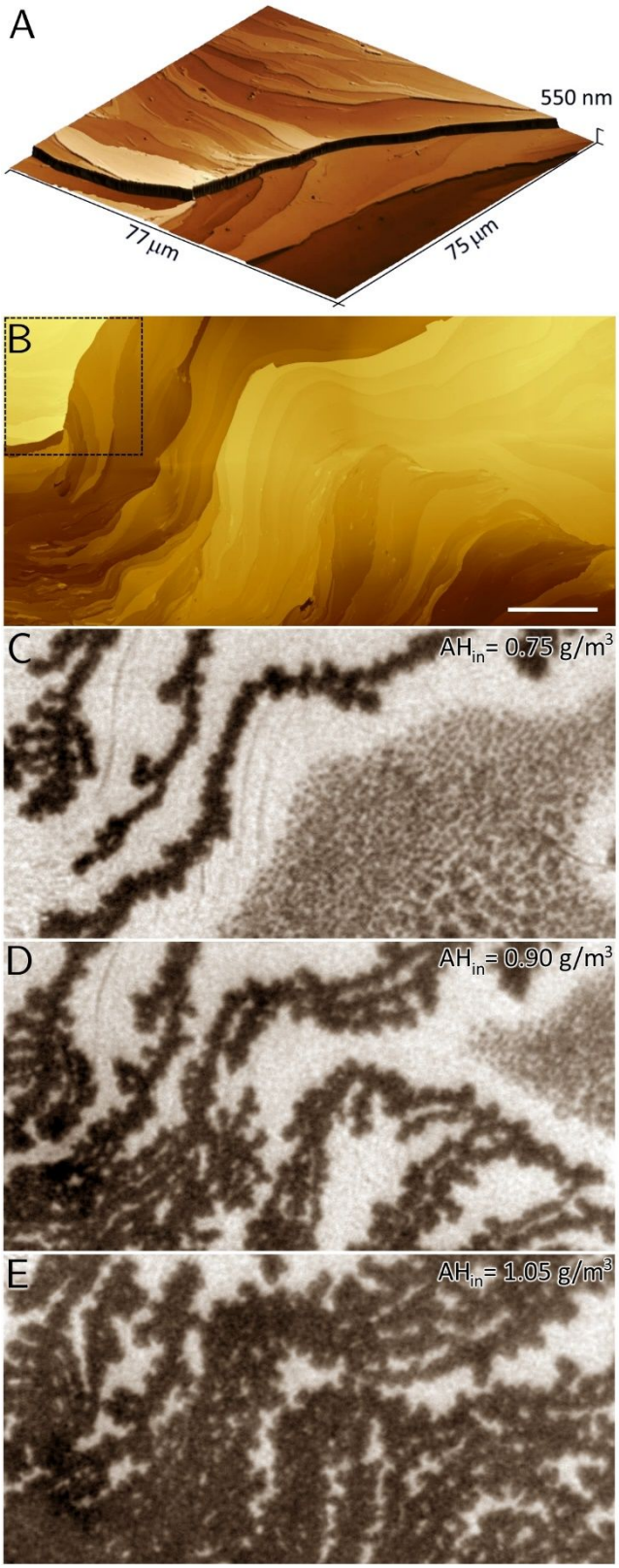

Fig. 2. Humidity-dependent rapid ice-growth patterns. (A) AFM image of feldspar substrate revealing surface steps of varying height. (B) Detailed map of surface topography assembled from multiple individual AFM frames. The dashed rectangle marks the field of view of the AFM image shown in (A) (scale bar 50 µm). (C-E) Optical images with the same FOV as (B), acquired shortly after rapid ice propagation has ceased, show ice growth patterns representative of the humidities AH_{in}= 0.75, 0.90, and 1.05 g/m^3, respectively. (See also Movies S4-S6).

A brief summary of the experimental method is provided here, while complete details can be found in the Electronic supplementary information (ESI†). Ice growth experiments are conducted inside a microliter mixing chamber. Here, feldspar substrates are exposed to cold and humid nitrogen at atmospheric pressure. The mixing chamber consists of a glass electrochemical AFM liquid cell (model ECFC, Bruker) with two inlet ports, one for cold dry N_2 and the other for humid N_2, that combine at the entrance to the sample chamber. This prevents mixing of cold and humid N_2 before they enter the chamber. An AFM (Multimode 8, Bruker) is stationed under a top-down optical microscopy stage with a 10× long-working-distance lens. Video microscopy data is recorded with an Infinity3-3URC 2.8 MP, 53 fps, color CCD camera. Microscopy substrates were mechanically split off from single crystals of K-feldspar (Orthoclase, $KAlSi_3O_8$, Yavapai County, Arizona, USA, vendor: VWR/Eric Miller) along the easy-cleavage plane (001).

Results and discussion

Two modes of ice growth on feldspar

To examine the onset of ice growth we cooled the feldspar sample to T≈ -30°C and subsequently exposed it to varying levels of humidity. Absolute humidity values (AH_{in}) provided hereafter represent estimates of the water content of the gas stream injected into the environmental chamber. (Note that after condensation and especially ice growth has started, the atmosphere in the microliter environmental chamber enters a non-equilibrium stage, in which the local humidity, especially near growing ice features, can be much lower than the given AH_{in} values). The video sequences in Fig. 1 reveal two humidity-dependent growth modes observed over identical surface regions. Just below saturation (AH_{in}= 0.45 g/m^3, Fig. 1B, Movie S1), few dispersed ice nuclei appear and grow slowly (< 5µm/s). Consistent with previous observations,[33] these ice crystals typically nucleate at the same surface sites when experiments are repeated at identical conditions.

At higher humidity (AH_{in}= 0.75 g/m^3, Fig. 1C, Movie S2), a different scenario unfolds. Immediately after humidity is introduced, the image darkens due to condensation of small water droplets that cover the surface. Then, darker features abruptly appear and elongate at speeds (≈ 2mm/s) far greater than observed for ice growth from vapor. These features often branch out producing patterns reminiscent of river systems. Simultaneously, a drainage area devoid of droplets evolves around these dark features as they continue to expand. Evidently, these dark features consume nearby water droplets, thus disclosing their icy nature: As during the Wegener-Bergeron-Findeisen process[37] in the atmosphere, within an admixture of liquid water and ice particles at subfreezing temperatures, water is expected to evaporate from the droplets and deposit onto the ice. A comparison between the frames of Fig. 1C with the AFM image of the same surface region (Fig. 1A), reveals that the dark ice bands emerge at surface steps of the feldspar

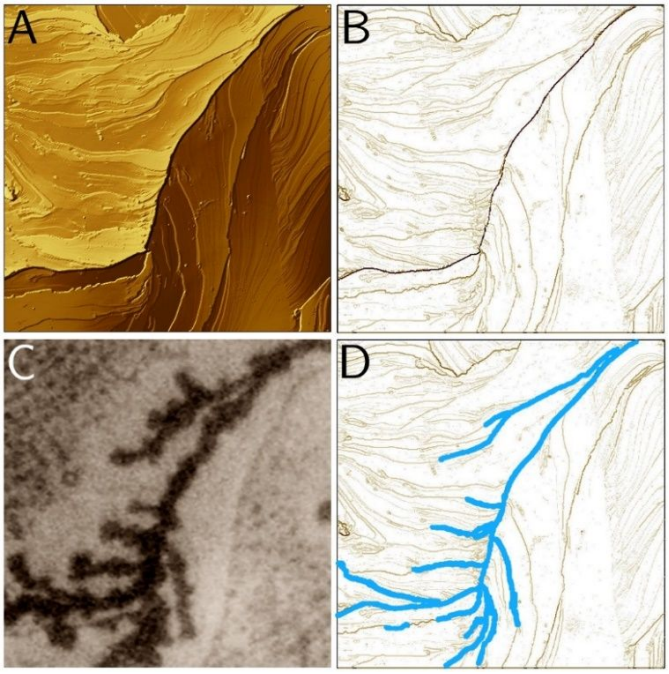

Fig. 3. Analysis of surface step segments. (A) A 100x100 µm² AFM image of the feldspar surface is shown in a mixed false color/shading presentation (Gwyddion) to visualize surface steps of large and small heights. (B) A step-edge height map derived from the image in (A), where darker colors are assigned to steps larger in height. This map is compared to an optical image (C), of the same surface region showing ice formation along step-edges, here at -30°C, AH_{in}= 0.75 g/m³. (D) Map based on (B) with ice-bearing step segments, as identified in (C), marked in blue. The heights and lengths of the ice-bearing and bare step segments are evaluated to produce the statistical distributions shown in Fig. 4.

substrate. The spatial relationship between ice structures and surface steps becomes strikingly obvious, when the optical and AFM data are superimposed as in Movie S3. The rapid ice propagation along surface steps terminates within seconds, but slow ice accretion onto existing ice bands continues until the experiment is aborted. From these irregularly-shaped ice structures one cannot deduce whether (100) microfacets are as crucial for ice nucleation at saturation, as reported for lower humidity.[33] The experiments analyzed in this paper were performed on the easy-cleavage plane (001). Similar ice bands along surface steps also develop on the other easy-cleavage plane of feldspar, (010), shown in Fig S4.

Humidity-dependent step icing

Can these unanticipated surface patterns provide clues to feldspar's superb ability to initiate ice? To understand the observed growth behavior, we examined the surface evolution at varying humidities (see Fig. 2). Before starting the growth experiments, we generated a topographical map of the same FOV to be examined by optical microscopy by stitching multiple 100 µm AFM images together (Fig. 2B and S2). During ice growth, the evolution of the surface was monitored optically. Typical ice growth patterns representative of different humidities, imaged shortly after rapid ice propagation has ceased, are shown in Fig. 2 C-E (and Movies S4-S6). There is a clear trend that as humidity increases more ice is being deposited. And again, the comparison with the AFM topography map reveals that the dark ice bands form along surface steps.

To investigate the steps' role during ice growth, we map optical images of ice-forming locations onto corresponding AFM topography data containing precise information about the steps' location and height. Figure 3 illustrates this mapping procedure for a 100 µm x 100 µm surface region, representing ≈9% of the total examined surface area, shown in Fig S3. The analysis scheme detects surface steps in the

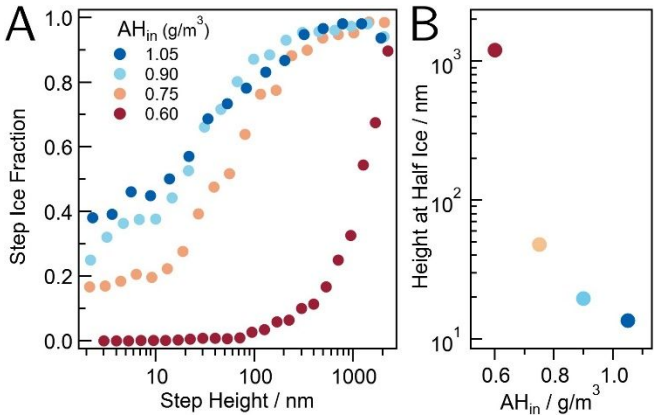

Fig. 4. Statistics of ice-bearing surface steps at -30°C. (A) Fraction of ice-bearing step segments as a function of their height for four different humidities. (B) Step height at half ice as a function of humidity – defined as the step height where half the total length of steps of that height bear ice.

AFM data (Fig. 3A) and breaks those up into segments of uniform height (Fig. 3B). A comparison with the corresponding optical image (Fig. 3C) is used to determine whether a given step segment bears ice or not (Fig. 3D). The height and ice-bearing information for all detected step segments is then evaluated.

The plot in Fig. 4A shows the fraction of ice-bearing step segments as a function of their height for four different humidities. For all examined humidities the fraction of ice-bearing steps increases with their height. There is also a clear trend that higher humidity increases the iced-step fraction. The plot of Fig. 4B shows that the step height at which half of the step population bears ice decreases monotonically with rising humidity. To have a 50% chance of bearing ice, a step must be taller than 1 µm at AH_{in}= 0.6 g/m³, but can be as small as 14 nm at AH_{in}= 1.05 g/m³.

Condensation and freezing at steps

Thus far we have established that surface steps dominate ice propagation on extended feldspar surfaces when humidity is raised above saturation. To assess surface steps' potential to promote ice formation in Earth's atmosphere we need to understand the underlying microscopic processes. Consider a surface step comprised of a small (010) facet, an easy-cleavage plane perpendicular to the main (001) feldspar surface (See Fig S2). Since the contact angle between water and orthoclase is ≈ 45° [38], a body of liquid water filling the bottom of a (010) step edge would have a nearly planar

surface (see Fig. 5A). This wedge-shaped water body has a vanishing net interface energy; hence its formation is not impeded by any nucleation barrier (see ESI†). Now we recall that in experiments where rapid ice propagation occurs, it is preceded by the condensation of small droplets of liquid water (Fig.1D, Movies S2-S6). According to the Kelvin equation, the local equilibrium vapor pressure above a spherical droplet with radius r is $p_v(r) = p_v(\infty)\exp[2\sigma v_m/(rRT)] \approx p_v(\infty)\exp[0.33/(r[\mu m]T[K])]$ [1], where $p_v(\infty)$ is the equilibrium vapor pressure above a planar water surface, σ the surface tension and v_m the molar volume of water, and R the molar gas constant. For convex droplets ($r>0$) $p_v(r)$ is always larger than $p_v(\infty)$. For example, the local equilibrium vapor pressure above a water droplet 500 nm wide at its base with a contact angle of ≈ 45° would be $p_v(r=0.5\mu m/\sqrt{2}) = p_v(\infty)\times 1.0038$, i.e., 0.38 % larger than above a planar surface. Since a gradient in local vapor pressure causes net diffusion from higher to lower pressure, the presence of a droplet near a (010) step would stabilize a water wedge along the bottom of the step (Fig. 5A). We can thus assume that, when droplets are nearby, most step edges are lined with liquid water, providing a continuous path along which ice can readily propagate via in-place freezing. Since this process does not involve long-range mass transport, it is much faster than the subsequent widening of the ice bands, which requires water molecules to diffuse through the atmosphere before they attach to the ice bands. The mechanism we are proposing here can be viewed as a special case of pore condensation and freezing [29,30] where in the absence of pores, their role is taken over by surface steps. Due to the geometry of step-and-terrace configurations prevalent on feldspar, i.e., the 90° angle between step and terrace, and a 45°wetting angle, a minimum humidity of RHw≈100 % is needed for surface steps to initiate condensation and freezing.

Can this proposed mechanism account for the observed trends of increased humidity and step height leading to higher fractions of ice-bearing steps? Consider the situation when ice has formed somewhere near a liquid water wedge (Fig. 5B). At this low temperature (T= -30°C), the vapor pressure in equilibrium with ice is much lower than the vapor pressure above the water wedge, which is close to the saturation vapor pressure $p_v(\infty)$ with respect to liquid water. The resulting gradient in local vapor pressure leads to a net mass flux from the water wedge towards the ice. Since water wedges have a nearly planar surface regardless of their size, the local equilibrium vapor pressure above them is constant, i.e. $p_v = p_v(\infty)$. As a consequence, in a given local environment, the evaporation rate, measured by volume per time and surface area, is independent of the wedge size. Hence the time it takes to completely drain a wedge through evaporation is roughly proportional to its initial size determined by the height of its host step. In addition, a larger wedge, by virtue of its larger water-feldspar interface, has a higher probability to cover a preferred ice nucleation site on the substrate with supercooled water. Thus, a water-wedge segment at a taller step has an increased probability to survive long enough to be itself turned into ice.

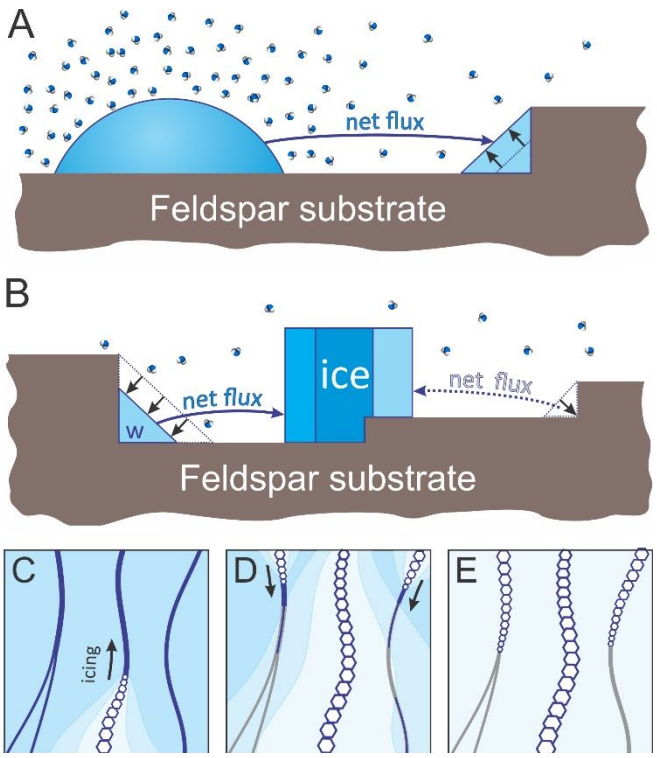

Fig. 5. Schematic of ice growth involving water condensation and freezing. (A) Initially, the presence of nearby droplets stabilizes a liquid water wedge residing at the lower side of a (010) step edge. (B) After ice has formed nearby, a net mass flux towards the ice drains the water wedges. Due to its larger water-holding capacity a wedge at a taller step is more likely to survive until turning itself into ice. (C-E) Example scenario of rapid ice propagation. (C) Initially, liquid water decorates the surface steps (dark blue), and all surface regions are covered by small water droplets (medium blue background). Ice just started to form on the center step, and propagates rapidly in the direction of the arrow. Denuded zones (few or no droplets, lighter shades of blue) develop. (D) The denuded zone expands, reaches neighboring steps, and starts to drain their water wedges. Step segments of little water-bearing capacity (bottom left) or near the iced center step (center right) become dry (gray). (E) Ice formation on the outer steps has stopped at the dry segments. All liquid water is consumed and ice grows exclusively via vapor deposition.

The high speed with which the ice spreads along steps, and the measured dependence of ice bearing on step height and humidity allowed us to infer that liquid water is involved in the ice formation process. A more direct method, i.e., direct imaging of liquid water at step edges, has previously been demonstrated at room temperature using various modes of atomic force microscopy.[39,40] Extending AFM imaging to supercooled water would be highly desirable because of AFM's superior spatial resolution compared to optical microscopy, however, possible sample modifications by the imaging tip and the high speed of freezing still represent formidable obstacles for such direct approach.

Surface steps compete for water during icing

The example scenario in Fig. 5 C-E illustrates how the processes described above interact when a stepped feldspar surface is exposed to cold supersaturated air, as during the experiments shown in Fig. 2 C-E. Initially, water from the air

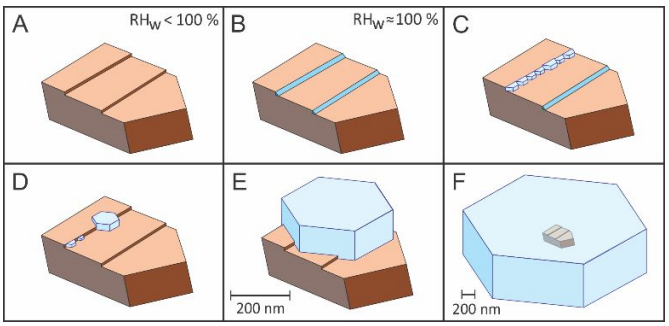

Fig. 6. Schematic of ice initiation on a stepped, cavity-free K-feldspar dust particle suspended in cold (-30°C) air that becomes supersaturated. (A) Initially, at RH_w <100%, a typical-size (≈500 nm wide) feldspar aerosol particle is assumed to be free of ice and water. Two of the many surface steps are shown as dark bands. (B) As humidity reaches RH_w ≈100%, liquid water condenses at the lower sides of the surface steps. (C) At one of the steps (the left one) water freezes. (D) The ice at the left step is an efficient sink for nearby water molecules. Via diffusion it drains all liquid water from the dust particle surface. Due to Ostwald ripening one ice crystal grows at the expense of its smaller neighbors. (E) The remaining ice crystal continues to grow as long as the surrounding air is supersaturated with respect to ice, and (F) quickly engulfs the dust particle on which it had nucleated. During the scenario depicted in A-F, water condenses at steps without having to overcome a nucleation barrier, thus facilitating subsequent ice formation.

condenses into continuous liquid water wedges along surface steps and subsequently into small liquid water droplets all over the surface (Fig. 5C). After ice has nucleated somewhere along the center step, it propagates rapidly in the direction of the arrow by freezing the wedge. The frozen segments grow laterally at the expense of nearby water droplets creating an expanding denuded zone, where the local humidity is below saturation. When the denuded zone reaches the neighboring steps (Fig. 5D) it starts draining their water wedges. Since the middle segment of the step on the right is closest to the ice bearing center step, its wedge evaporates at a higher rate and soon becomes completely dry. The step on the left splits into two smaller steps, whose wedges carry less water and are therefore depleted earlier. Ice propagation at these outer steps (arrows in Fig. 5D) comes to a halt when the freezing front reaches their dry segments (Fig. 5E). After all liquid water is consumed, ice continues to grow slowly via vapor deposition from the air. A higher inlet humidity, i.e., an increased water supply, counteracts the spreading of denuded zones and reduces the rates at which the water wedges evaporate, explaining the measured trend (Fig. 4) that higher humidity increases the iced-step fraction. Injecting high humidities and interpreting ice patterns observed on extended surfaces allowed us to establish the nature of a step-enhanced growth mode. In the following section we apply this new insight into the involved microscopic processes to realistic atmospheric conditions.

Step-enhanced ice formation on aerosols

As mentioned in the context of Fig. 5A, a humidity of only RH_w≈ 100 % is needed to stabilize a liquid water wedge at an individual feldspar surface step. To assess how water wedges at steps effect atmospheric ice formation, we discuss the scenario of a typical-size[5,12] (≈500 nm wide) cavity-free feldspar aerosol particle suspended in cold (≈-30°C) air that becomes slowly saturated, e.g., by cooling in an updraft or by mixing with a nearly-saturated air parcel of a different temperature.[1,2,41,42] For our scenario we consider the case that the humidity does not rise at least for a few seconds above RH_w≈ 100.4 %, a value below which any liquid water droplet that fits onto on a 500 nm wide feldspar terrace would be unstable (see section "Condensation and freezing at steps"). (Above RH_w= 100% the rise in humidity is expected to decelerate due to the onset of water drainage by neighboring cloud condensation nuclei.) We further only consider the nontrivial case that, due to its atmospheric history, the feldspar particle is initially devoid of ice. (An ice-bearing particle could simply grow via attachment of water molecules from vapor at RH_{ice}> 100%, without any need for involvement of the feldspar surface). Lacking cavities that would allow condensation below saturation,[29,30,35,36] the feldspar particle is expected to remain free of liquid water below saturation, i.e., at RH_w <100% (Fig. 6A). For simplicity, just two surface steps are shown, typically representing hundreds of steps of various heights and orientations on a dust particle surface. Since (001) and (010) planes are the two easiest cleavage planes, configurations of (010) step segments on a (001) facet, or (001) step segments on a (010) facet, are expected to be ubiquitous on a K-feldspar dust particle. At the lower side of these surface steps, as explained in the discussion of Fig. 5, liquid water will condense into a wedge with a nearly planar surface at almost exactly RH_w =100% (Fig. 6B), while water deposited onto the (flat) surface terraces evaporates or diffuses to a step edge. Pruppacher & Klett[1] (see Fig. 9-11) and Fletcher[43] estimate that a humidity of RH_w> 130 % is required to achieve measurable nucleation rates of water droplets with contact angles of 45° on a planar insoluble substrate. But even without a detailed discussion of the droplet-nucleation rate, which depends on multiple difficult-to-constrain quantities, a simpler argument can be made by considering the largest and thus most stable droplet on a 500 nm wide terrace, which measures 500 nm at its base, and (with a contact angle of ~ 45°) has a radius of 500/√2 nm ~350 nm. According to the Kelvin equation, such a droplet needs at least a humidity of RH_w= 100.38 % to be stable. Hence, below RH_w≈ 100.38 % water will be confined to step-edges, the only locations where water condensates can be stable due to a large enough radius of surface curvature. Owing to the ice-nucleation efficiency of K-feldspar, the supercooled water will start to freeze within seconds at some location within a water wedge and then rapidly convert this wedge into a band of polycrystalline ice (Fig. 6C). Now we recall that the step analysis of Fig. 4 revealed how efficiently steps are drained by their larger neighbors even at higher humidities and over distances much larger than the dimensions of this aerosol particle. Thus, due to their proximity on this small aerosol particle, all remaining liquid water wedges are quickly drained by a net water mass flux toward the ice band (Fig. 6D). Over longer timescales,

smaller ice crystallites within the band are consumed by one (or a few) bigger ice crystal via Ostwald ripening. The ice crystal(s) will grow by incorporating water drained from the surrounding air (Fig. 6E). Since the overall humidity of the surrounding air parcel is assumed to be RH_w ≈100% in this scenario, which at T=-30°C represents a large supersaturation with respect to ice (RH_{ice} ≈134%),[44] the ice crystal keeps growing by drawing water vapor from the surrounding air and will eventually envelope the feldspar dust particle (Fig. 6F). If the surrounding atmosphere remains supersaturated with respect to ice, this crystal continues to grow, and can become heavy enough to precipitate. Such competitive process produces the often observed single-crystal ice precipitates collected from the atmosphere as snowflakes.[1,2,45] In short, this scenario is enabled by surface steps on airborne feldspar dust that eliminate the energy barrier to form extended condensates of liquid water, which then, by being in contact with K-feldspar at temperatures below -20°C, readily initiate ice formation.[16,18,19]

Conclusions

The combination of optical and AFM imaging used in this paper yields insight into ice growth on minerals at scales not seen before. The experiments performed at atmospheric pressure reveal that, when cold air (T≈-30°C) becomes supersaturated (RH_w>100%), ice growth on the main cleavage plane of K-feldspar initiates at surface steps. Rapid spreading of ice along those steps, and its dependence on step height and humidity implies that ice growth proceeds via water condensation and freezing.[29,30,35,36] By allowing the formation of extended condensates of supercooled water without having to overcome an energy barrier, this mechanism facilitates subsequent ice formation. We propose this process to occur in Earth's atmosphere when air colder than -20°C, the temperature below which ubiquitous feldspar aerosols are efficient ice nuclei,[16,18,19] becomes saturated. This condition arises, for example, upon cooling in updrafts or when nearly-saturated air parcels of different temperatures mix,[1,2,41,42] if reaching saturation is not prevented by extensive pore condensation and freezing on cavity-containing aerosols.[29,30,35,36] Step-facilitated ice formation is likely to occur on other hydrophilic materials, if their surfaces contain step edges with active ice-nucleation sites at their bottom. Further studies are needed to quantify what impact surface steps on solid aerosols might have on the rate of atmospheric ice formation, and thus on weather and global climate. Nevertheless, our results provide additional support of recent arguments[19,30] that surface morphology is more important than previously recognized for ice evolution under atmospheric conditions. Hence, morphological surface properties, like the presence of surface steps of a suitable height,[46] favorably-arranged cavities,[30] or perthitic texture in alkali feldspars,[19] should be considered, besides particle size[5] and wetting angle,[47] when developing ice-nucleation schemes for climate predictions.[4,5,47] Further advances in understanding morphology's effect on ice nucleation are likely to arise if microscopy techniques can be adapted for high-resolution experiments on pore condensation and freezing as well as on freezing of supercooled droplets. Finally, the rapid spreading of ice we observed on feldspar, is expected to play a role in other circumstances where extended surfaces, covered with continuous networks of steps or grooves, are exposed to a supersaturated atmosphere, providing a microscopy-based argument for avoiding rough surfaces with large steps or grooves in efforts to prevent aircraft icing.[48,49]

Conflicts of interest

There are no conflicts to declare.

Acknowledgements

We thank Norman C. Bartelt, Erika L. Roesler, and Lauren Wheeler for insightful discussions. This work was supported by the Sandia Laboratory Directed Research and Development Program. Sandia National Laboratories is a multi-mission laboratory managed and operated by National Technology and Engineering Solutions of Sandia LLC, a wholly owned subsidiary of Honeywell International Inc. for the U.S. Department of Energy's National Nuclear Security Administration under contract DE-NA0003525.

Notes

[i] Throughout this manuscript we use the term "ice formation" for the entire process that produces ice, i.e., ice nucleation and growth and/or freezing.

References

1 H. R. Pruppacher and J. D. Klett, *Microphysics of clouds and precipitation*. 2nd edn, Kluwer Academic Publishers, Dordrecht, 1997.
2 R. R. Rogers and M. K. Yau, *A short course in cloud physics*. 3rd edn, Pergamon Press, 1989.
3 U. Lohmann and J. Feichter, *Atmos. Chem. Phys.*, 2005, **5**, 715-737.
4 A. Gettelman, X. Liu, D. Barahona, U. Lohmann and C. Chen, *J. Geophys. Res.-Atmos.*, 2012, **117**, D20201.
5 P. J. DeMott, A. J. Prenni, X. Liu, S. M. Kreidenweis, M. D. Petters, C. H. Twohy, M. S. Richardson, T. Eidhammer and D. C. Rogers, *Proc. Natl. Acad. Sci.*, 2010, **107**, 11217-11222.
6 I. Tan, T. Storelvmo and M. D. Zelinka, *Science*, 2016, **352**, 224-227.
7 K. M. Lau and H. T. Wu, *Geophys. Res. Lett.*, 2003, **30**, 5.
8 J. Mulmenstadt, O. Sourdeval, J. Delanoe and J. Quaas, *Geophys. Res. Lett.*, 2015, **42**, 6502-6509.
9 G. Vali, P. J. DeMott, O. Mohler and T. F. Whale, *Atmospheric Chemistry and Physics*, 2015, **15**, 10263-10270.
10 Z. A. Kanji, L. A. Ladino, H. Wex, Y. Boose, M. Burkert-Kohn, D. J. Cziczo and M. Krämer, *Meteorological Monographs*, 2017, **58**, 1.1-1.33.

11 C. Hoose and O. Mohler, *Atmospheric Chemistry and Physics*, 2012, **12**, 9817-9854.
12 M. Kamphus, M. Ettner-Mahl, T. Klimach, F. Drewnick, L. Keller, D. J. Cziczo, S. Mertes, S. Borrmann and J. Curtius, *Atmospheric Chemistry and Physics*, 2010, **10**, 8077-8095.
13 K. A. Pratt, P. J. DeMott, J. R. French, Z. Wang, D. L. Westphal, A. J. Heymsfield, C. H. Twohy, A. J. Prenni and K. A. Prather, *Nature Geoscience*, 2009, **2**, 397-400.
14 D. J. Cziczo, K. D. Froyd, C. Hoose, E. J. Jensen, M. H. Diao, M. A. Zondlo, J. B. Smith, C. H. Twohy and D. M. Murphy, *Science*, 2013, **340**, 1320-1324.
15 C. Hoose, J. E. Kristjansson, J. P. Chen and A. Hazra, *J. Atmos. Sci.*, 2010, **67**, 2483-2503.
16 J. D. Atkinson, B. J. Murray, M. T. Woodhouse, T. F. Whale, K. J. Baustian, K. S. Carslaw, S. Dobbie, D. O/'Sullivan and T. L. Malkin, *Nature*, 2013, **498**, 355-358..
17 J. D. Yakobi-Hancock, L. A. Ladino and J. P. D. Abbatt, *Atmospheric Chemistry and Physics*, 2013, **13**, 11175-11185.
18 L. Kaufmann, C. Marcolli, J. Hofer, V. Pinti, C. R. Hoyle and T. Peter, *Atmospheric Chemistry and Physics*, 2016, **16**, 11177-11206.
19 T. F. Whale, M. A. Holden, A. N. Kulak, Y. Y. Kim, F. C. Meldrum, H. K. Christenson and B. J. Murray, *Phys. Chem. Chem. Phys.*, 2017, **19**, 31186-31193.
20 C. E. Jordan, J. E. Dibb, B. E. Anderson and H. E. Fuelberg, *J. Geophys. Res.-Atmos.*, 2003, **108**, 1-10.
21 R. C. Sullivan, S. A. Guazzotti, D. A. Sodeman and K. A. Prather, *Atmospheric Chemistry and Physics*, 2007, **7**, 1213-1236.
22 D. A. Knopf, P. A. Alpert, B. Wang, R. E. O'Brien, S. T. Kelly, A. Laskin, M. K. Gilles and R. C. Moffet, *Journal of Geophysical Research: Atmospheres*, 2014, **119**, 10,365-310,381.
23 T. Koop and N. Mahowald, *Nature (UK)*, 2013, **498**, 302-303.
24 P. J. DeMott, O. Mohler, O. Stetzer, G. Vali, Z. Levin, M. D. Petters, M. Murakami, T. Leisner, U. Bundke, H. Klein, Z. A. Kanji, R. Cotton, H. Jones, S. Benz, M. Brinkmann, D. Rzesanke, H. Saathoff, M. Nicolet, A. Saito, B. Nillius, H. Bingemer, J. Abbatt, K. Ardon, E. Ganor, D. G. Georgakopoulos and C. Saunders, *Bulletin of the American Meteorological Society*, 2011, **92**, 1623-1635.
25 I. Coluzza, J. Creamean, M. J. Rossi, H. Wex, P. A. Alpert, V. Bianco, Y. Boose, C. Dellago, L. Felgitsch, J. Frohlich-Nowoisky, H. Herrmann, S. Jungblut, Z. A. Kanji, G. Menzl, B. Moffett, C. Moritz, A. Mutzel, U. Poschl, M. Schauperl, J. Scheel, E. Stopelli, F. Stratmann, H. Grothe and D. G. Schmale, *Atmosphere*, 2017, **8**, 28.
26 A. Welti, Z. A. Kanji, F. Luond, O. Stetzer and U. Lohmann, *J. Atmos. Sci.*, 2014, **71**, 16-36.
27 T. Bartels-Rausch, V. Bergeron, J. H. E. Cartwright, R. Escribano, J. L. Finney, H. Grothe, P. J. Gutierrez, J. Haapala, W. F. Kuhs, J. B. C. Pettersson, S. D. Price, C. I. Sainz-Diaz, D. J. Stokes, G. Strazzulla, E. S. Thomson, H. Trinks and N. Uras-Aytemiz, *Rev. Mod. Phys.*, 2012, **84**, 885-944.
28 D. A. Knopf, P. A. Alpert and B. B. Wang, *ACS Earth Space Chem.*, 2018, **2**, 168-202.
29 C. Marcolli, *Atmospheric Chemistry and Physics*, 2014, **14**, 2071-2104.
30 R. O. David, C. Marcolli, J. Fahrni, Y. Qiu, Y. A. Perez Sirkin, V. Molinero, F. Mahrt, D. Brühwiler, U. Lohmann and Z. A. Kanji, *Proc. Natl. Acad. Sci.*, 2019, **116**, 8184-8189.
31 F. Zimmermann, S. Weinbruch, L. Schutz, H. Hofmann, M. Ebert, K. Kandler and A. Worringen, *J. Geophys. Res.-Atmos.*, 2008, **113**, D23204.
32 B. Wang, D. A. Knopf, S. China, B. W. Arey, T. H. Harder, M. K. Gilles and A. Laskin, *Phys. Chem. Chem. Phys.*, 2016, **18**, 29721-29731.
33 A. Kiselev, F. Bachmann, P. Pedevilla, S. J. Cox, A. Michaelides, D. Gerthsen and T. Leisner, *Science*, 2016.
34 V. Pinti, C. Marcolli, B. Zobrist, C. R. Hoyle and T. Peter, *Atmospheric Chemistry and Physics*, 2012, **12**, 5859-5878.
35 H. K. Christenson, *Crystengcomm*, 2013, **15**, 2030-2039.
36 N. Fukuta, *J. Atmos. Sci.*, 1966, **23**, 741-750.
37 A. Korolev, *J. Atmos. Sci.*, 2007, **64**, 3372-3375.
38 C. Karagüzel, M. F. Can, E. Sönmez and M. S. Çelik, *Journal of Colloid and Interface Science*, 2005, **285**, 192-200.
39 A. Verdaguer, G. M. Sacha, M. Luna, D. Frank Ogletree and M. Salmeron, *J. Chem. Phys.*, 2005, **123**, 8.
40 M. Cardellach, A. Verdaguer, J. Santiso and J. Fraxedas, *J. Chem. Phys. (USA)*, 2010, **132**, 7.
41 H. Morrison, G. de Boer, G. Feingold, J. Harrington, M. D. Shupe and K. Sulia, *Nature Geoscience*, 2012, **5**, 11-17.
42 A. Korolev and G. Isaac, *Quarterly Journal of the Royal Meteorological Society*, 2003, **129**, 19-38.
43 N. H. Fletcher, *The physics of rainclouds. Cambridge University Press*, New York, *1962*.
44 D. M. Murphy and T. Koop, *Quarterly Journal of the Royal Meteorological Society*, 2005, **131**, 1539-1565.
45 F. C. Frank, *Contemp. Phys.*, 1982, **23**, 3-22.
46 K. Thürmer and S. Nie, *Proceedings of the National Academy of Sciences*, 2013, **110**, 11757-11762.
47 Y. Wang, X. Liu, C. Hoose and B. Wang, *Atmospheric Chemistry and Physics*, 2014, **14**, 10411-10430.
48 R. W. Gent, N. P. Dart and J. T. Cansdale, *Philos. Trans. R. Soc. Lond. Ser. A-Math. Phys. Eng. Sci.*, 2000, **358**, 2873-2911.
49 M. J. Kreder, J. Alvarenga, P. Kim and J. Aizenberg, *Nat. Rev. Mater.*, 2016, **1**, 15.